Nanoscale

Effect of (3-Aminopropyl)triethoxysilane on dissolution of silica nanoparticles synthesized via reverse micro emulsion

Journal:	*Nanoscale*
Manuscript ID	NR-ART-03-2022-001190.R1
Article Type:	Paper
Date Submitted by the Author:	11-May-2022
Complete List of Authors:	Kang, Hyunho; University of Minnesota Lee, Jihyeon; University of Minnesota Department of Mechanical Engineering, Mechanical Engineering O'Keefe, Tana; University of Minnesota Tuga, Beza; State University of New York at Plattsburgh, Chemistry Hogan, Jr., Christopher; University of Minnesota Department of Mechanical Engineering, Mechanical Engineering Haynes, Christy; University of Minnesota,

Effect of (3-Aminopropyl)triethoxysilane on dissolution of silica nanoparticles synthesized via reverse micro emulsion

Hyunho Kang,[†] Jihyeon Lee,[‡] Tana O'Keefe, [†] Beza Tuga, [†] Christopher. J. Hogan Jr, [‡] Christy L. Haynes[†]

[†]Center for Sustainable Nanotechnology, Department of Chemistry, University of Minnesota, 207 Pleasant Street S.E., Minneapolis, Minnesota 55455, United States

[‡]Department of Mechanical Engineering University of Minnesota, Minneapolis, MN, 55455, United States

Abstract

Silica nanomaterials have been studied based on their potential applications in a variety fields, including biomedicine and agriculture. A number of different molecules have been condensed onto silica nanoparticles' surfaces to present the surface chemistry needed for a given application. Among those molecules, (3-aminopropyl)triethoxysilane (APS) is one of the most commonly applied silanes used for nanoparticle surface functionalization to achieve charge reversal as well

as to enable cargo loading. However, the colloidal stability of APS-functionalized silica nanoparticles has not been thoroughly studied, which can be problematic when the high reactivity of amine groups is considered. In this study, four different types of silica nanoparticles with varied location of added APS have been prepared via reverse a micro emulsion process, and their colloidal stability and dissolution behavior have been investigated. Systematic characterization has been accomplished using transmission electron microscopy (TEM), silicomolybdic acid (SMA) spectrophotometric assay, nitrogen adsorption−desorption surface area measurement, and aerosol ion mobility-mass spectrometry to track the nanoparticles' physical and chemical changes during dissolution. We find that when APS is on the interior of the silica nanoparticle, it facilitates dissolution, but when APS is condensed both on the interior and exterior, only the exterior siloxane bonds experience catalytic hydrolysis, and the interior dissolution is dramatically suppressed. The observation and analyses that silica nanoparticles show different hydrolysis behaviors dependent on the location of the functional group will be important in future design of silica nanoparticles for specific biomedical and agricultural applications.

Introduction

Surface functionalization of silica nanoparticles has been an essential part of the platform preparation, improving stability and transformation, especially for nanoparticle applications such in drug delivery[1–3] and diagnostic bioimaging.[4,5] In these applications, surface functionalization is typically performed (1) to enhance colloidal stability of the carrier nanoparticles by bypassing or mitigating aggregation and degradation in complex media[6,7] or (2) to improve nanoparticle targeting capacity by promoting cell permeation or a specific ligand-receptor interaction on cells of interest.[8,9] However, despite years of research and development, the achievements in this area have been moderate, largely due to incomplete or unpredictable stability of the nanoparticles when exposed to media.[10] In parallel to biomedical applications, silica nanoparticles have also been considered for agricultural applications, as the nanoparticles can function as nutrient carriers[11] or act as fertilizers themselves, delivering silicic acid or related molecules.[12,13] In biomedical applications, surface functionalization has also been applied in various ways for efficient uptake and desired colloidal stability.[14] Unfortunately, a similar disadvantage challenges the utility of silica nanoparticles in both fields, namely nanoparticle accumulation after performance, which arouses concerns about the safety of these applications.[15,16] Understanding the role and effect of

surface functional groups on the colloidal behavior of the nanoparticles, and hydrolysis in particular, can be the key to move forward to a more stable and robust nanoparticle application platform.

(3-aminopropyl)triethoxysilane (APS) is one of the most common and widely used silanes for surface modification of silica nanoparticles.[17] Termination with a primary amine group upon silane condensation generates a positive charge in neutral and weakly acidic aqueous suspension which is usually a charge reversal, as the original silanol group carries a negative electric potential in suspension.[18] Furthermore, this amine group serves as a coupling agent for many common organic reactions, enabling various types of more advanced functionalization.[19–21] The other widely known characteristic of APS is its catalytic behavior for the hydrolysis and condensation of siloxane bonds, and in some cases, this can offer a surface modification strategy where no water is needed and uniform surface coating is achieved.[22–24] When contacting water, APS can induce amine-catalyzed hydrolysis of the O-Si-O linkage, and this, in many cases, can be a problem as it can interfere with homogeneous surface functionalization. From another perspective, this feature can be exploited to hydrolyze the nanoparticle during synthesis to achieve a specific morphology or to design a more bio-friendly silica nanoparticle.[25] For example, in one study, APS-containing

silica nanospheres were synthesized and applied to plants to rapidly supply silicic acid, promoting growth and resistance to a fungal disease.[26] However, even in the *in vitro* dissolution study, APS did not take the nanoparticle to the point of complete dissolution, only to a hollow-shell formation by facilitating inner region hydrolysis. This might be attributed to the localization of the APS inside the nanoparticles, the difference in the degree of condensation, or another factor. Overall, it is obvious that proposing a strategic way to achieve complete dissolution of silica nanoparticles would be desirable for many applications where avoiding bioaccumulation is advantageous. With this goal in mind, this work explores silica nanoparticle hydrolysis and dissolution catalyzed by the functional group APS.

In this study, using a reverse-micro emulsion wet synthesis method, APS-containing silica nanoparticles were prepared to investigate their hydrolysis behaviors with the goal of achieving complete nanoparticle dissolution. APS molecules were incorporated within the silica network covalent structure either at the particle interior (core), exterior (shell), or both interior and exterior regions of the nanoparticles, and each nanoparticles' aqueous dissolution patterns were analyzed in multiple ways. Depending on the nanoparticle preparation conditions, the molar ratio of tetraethyl orthosilicate (TEOS), the main silica precursor, to APS varied from around 70 to 22, and

none of the nanoparticle types prepared resulted in complete hydrolysis. Interestingly, each type, with average diameters of roughly 47 nm, showed very distinct dissolution behavior dependent on the location where APS is condensed during the nanoparticle preparation in reverse-micro emulsion. To explore the dissolution patterns, this work employs electron microscope imaging, silicomolybdic acid spectrophotometric assays, dynamic light scattering, nitrogen adsorption-desorption surface area measurement, and ion mobility-mass spectrometry. The combined results showed that APS-driven hydrolysis is localized within the region where APS is present, and especially, the APS on the shell induced minimal density changes after the hydrolysis, despite the existence of APS in the inner region of the silica nanoparticles. The experiments and analyses yield fundamental insights on the hydrolysis behaviors of silica nanoparticles in aqueous media, which will be beneficial in future design of silica nanoparticles for specific applications in biomedical and agricultural applications.

Experimental Method

Materials. Tetraethyl orthosilicate (TEOS, reagent grade 98%), (3-aminopropyl)triethoxysilane (APS, 99%), chlorotrimethylsilane (TMS, 98%), ammonium molybdate tetrahydrate, oxalic acid,

sodium sulfite (anhydrous), cyclohexane (anhydrous), Triton X-100, 1-hexanol (anhydrous), 4-methylaminophenol sulfate, and silicon standard solution (1000 ppm) were purchased from Sigma-Aldrich (St. Louis, MO). 2-[methoxy(polyethyleneoxy)$_{9\text{-}12}$propyl]trimethoxysilane (PEG, molecular weight 591-723 g/mol) was purchased from Gelest (Morrisville, PA). All chemicals were used without further purification.

Solid Spherical Silica Nanoparticle Preparation. Four different silica nanoparticles were synthesized using a reverse microemulsion method.[27] In general, two silica precursor molecules, TEOS (tetraethyl orthosilicate) and APS ((3-aminopropyl)triethoxysilane), were used. TEOS was used as the main silica precursor molecule for all four particles, and APS was added at different steps with varied amounts during preparation, depending on the nanoparticle types. The first particle was prepared with only TEOS ((TEOS)$_{Core}$). In the 150 mL Erlenmeyer flask, 19.25 g of Triton x-100, 18 mL 1-hexanol, and 76 mL of cyclohexane were added and mixed well. Then, the flask was transferred to a stir plate and stirred at 450 rpm with a stir bar. 30 minutes later, 4.8 mL of water was added dropwise under continuous stirring. 10 minutes later, 1 mL of concentrated NH_4OH was added and stirred for 2 hours. Then, 1 mL of TEOS was added dropwise. The solution

was stirred for 24 hours at room temperature. For the second particle, $(TEOS)_{core}(APS)_{shell}$, the procedure was the same as that of $(TEOS)_{core}$, but after 24 hours of stirring with TEOS, 17.5 μL of APS was added with 10 hours of additional stirring. For the third particle, $(TEOS+APS)_{core}$, when TEOS was added, 35 μL of APS was added at the same time followed by 24 hours of stirring. For the last particle, $(TEOS+APS)_{core}(APS)_{shell}$, 35 μL of APS was added together when TEOS was added followed by 24 hours of stirring. Then, 17.5 μL of APS was added with 10 hours of further stirring. The purification procedure was the same for all particles: the stirring was stopped, and 200 mL of ethanol was added and stirred with a rod to break the micro emulsion. The suspension was centrifuged 6 times for 20 minutes at 65,400 relative centrifugal force (RCF). Each pellet obtained was re-dispersed in ethanol with sonication until all pellets disappeared. The final pellets were dispersed in 99% ethanol, filtered through a syringe filter (GHP membrane 0.45 μm syringe filters), and stored in the refrigerator until use.

Transmission Electron Microscopy (TEM). TEM images were taken with FEI Tecnai T12 at 120 kV. First, the particles in 99% ethanol were dried by rotary evaporator, and the weight of the dried and powdered particles was measured to suspend the particles in 99% ethanol at an approximate

concentration of 1 mg/mL with sonication. The nanoparticles were deposited onto Formvar/carbon-coated copper grids (Ted Pella, Inc., Redding, CA) by dipping the grids into the prepared suspension for 2 seconds. The grids were dried in air. For the aged particles, the samples were prepared in the same way, but after incubation the particles were washed in ethanol several times to remove dissolved silicic acid. During measurement, the nanoparticles were well-distributed on the grid, and at least 400 nanoparticles per type were analyzed using ImageJ for the diameter measurement.

Surface Area Measurements. Nitrogen adsorption−desorption isotherms with Brunauer−Emmett−Teller (BET) and Barrett-Joyner-Halenda (BJH) pore size and volume analyses were used to measure the surface area and pore volume of the silica nanoparticles. Each particle in ethanol was dried and powdered, then the sample powder was degassed at a pressure of 15 μm Hg at 60 ˚C for 800 minutes prior to analysis. For each powder sample, at least 100 mg was analyzed (Micromeritics ASAP 2020, Norcross, GA). For the aged particles, the samples were prepared in the same way, but after incubation the particles were washed in ethanol several times to remove non-particulate monomers or oligomers.

ζ-Potential Measurements Brookhaven ZetaPALS Zeta-Potential Analyzer (Holtsville, NY) was used to measure the surface electric potential in ethanol. The particles prepared as powder form were dispersed in ethanol at the concentration of 1 mg/mL. The suspensions were sonicated for dispersion before measurement. Average values were obtained from 10 independent measurements.

Silicomolybdic Acid (SMA) Spectrophotometric Assay Two assay solutions were prepared for the assay that quantifies silica dissolution.[28] The assay solution A was prepared by mixing 30 mL of concentrated hydrochloric acid into 400 mL of deionized water. Then, 10 g of ammonium molybdate tetrahydrate was added and dissolved. The solution was diluted to 500 mL with deionized water. The assay solution B was prepared by mixing 100 mL of concentrated sulfuric acid into 800 mL of deionized water. Then, 20 g of oxalic acid, 6.67 g of 4-methylaminophenol sulphate, and 4 g of anhydrous sodium sulfite were added and dissolved. The solution was diluted to 1L with deionized water. For the assay, each nanoparticle type in powdered form was dispersed in ultrapure water at 150 mg/L with sonication. The suspensions were incubated at room

temperature. At each measurement timepoint, 0.1 mL of the suspension was taken out and diluted with 1.6 mL of ultrapure water. Then, 0.15 mL of the assay solution A was added. After 10 minutes, 0.75 mL of the assay solution B was added, and the solution sat at room temperature for 2 hours. The optical density of the solutions at 810 nm were measured with a UV−vis spectrometer (Ocean Optics, Largo, FL) to quantify the concentration of reduced silicomolybdic acid, also known as the molybdenum blue complex. The silicic acid concentration was calculated by comparison of the optical densities of the sample mixtures with those of the diluted silicon standard solutions.

Solid-State ^{29}Si-MAS-NMR. Bruker AVANCETM III HD 400 WB400 spectrometer, with a 7 mm Bruker BL-7 probe at a sample spinning rate of 5 kHz was used for Solid-State magic angle spinning−nuclear magnetic resonance (MAS NMR) spectra at room temperature. The reference was tetramethylsilane. The single pulse ^{29}Si spectra were acquired using pulses of 3.5 μs corresponding to a flip angle of $3\pi/4$ rad and a recycle delay of 240 s and with a reference of

tetramethylsilane. The ^{1}H to ^{13}C cross-polarization spectra were acquired by using a 90 pulse for ^{1}H of 5 μs, a contact time of 5 ms, and a recycle of 3 s and this was referenced to adamantine.

Aerosol Ion Mobility-Mass Spectrometry. Aerosol Ion Mobility-Mass Spectrometry (IM-MS) is a characterization technique for nebulized particles in the gas phase (in an aerosol), with efforts made to preserve the particle size distribution by ensuring minimal non-volatile residue and minimizing non-specific aggregation.[29] In aerosol IM-MS, particles are first examined by differential mobility analysis, yield their mobility-equivalent size, and second centrifugal aerosol mass analysis[30], yielding their masses. Combined, measurements provided the nanoparticle size distribution and mass as a function of size (and possibly a multidimensional size-mass distribution function), and hence can be used to quantify particle density changes. For aerosol IM-MS of silica nanoparticle suspensions, both fresh and aged for 3 days (both in ethanol), samples were diluted with ultrapure water with a dilution ratio of 1:200 directly before measurements. For the samples aged, the suspensions were incubated in pure water at the concentration of 400 ppm for 3 days, washed, dried, then transferred to ethanol at a concentration of 0.9 mg/mL. The fresh samples in ethanol have the same concentration as the aged samples. Each sample was aerosolized by a

nanoparticle nebulizer (NPN, Kanomax FMT)[31] with a liquid feedrate of 1 mL min^{-1} using a direct injection mode. Aerosolized particles were first analyzed to determine their mobility diameter distributions using a scanning mobility particle spectrometer (SMPS)[32] consisting of a soft x-ray neutralizer,[33] a nano differential mobility analyzer (nano DMA, 3085, TSI inc)[34], and a condensation particle counter (CPC, 3776, TSI Inc). The aerosol flowrate was 0.3 L min^{-1} and the sheath flowrate was 3.0 L min^{-1} within the DMA. Second, particles were analyzed with the DMA coupled to aaerosol particle mass analyzer (APM, 3602, Kanomax Inc)-CPC (3650, Kanomax FMT)[30,35,36] to obtain the density distribution, again using soft X-ray for particle ionization prior to passage into the DMA. The aerosol flowrate through the system was 0.6 L min^{-1}, the sheath flow rate of the DMA was 6.0 L min^{-1}, and the rpm of the APM was 13000.

Result and Discussion

Solid spherical silica nanoparticles were prepared via a reverse micro emulsion method. In the method, each water droplet surrounded by two different surfactants acts as a small micro reactor, producing a single nanoparticle. The size of the droplet largely determines the size of the nanoparticles produced, and in most cases, due to the homogeneous size of the droplet, the

resulting particles are quite monodisperse, enabling efficient comparison among different nanoparticle types in this study. Tetraethyl orthosilicate (TEOS) was used as a main precursor molecule, and 3-aminopropyltriethoxysilane (APS) was applied during preparation as a secondary precursor molecule to vary the dissolution behaviors of the nanoparticles. The nanoparticle prepared with only TEOS was named $(TEOS)_{core}$, and this nanoparticle represents traditional silica nanoparticles without additional surface functionalization. The second nanoparticle $(TEOS)_{core}(APS)_{shell}$ was produced the same way as the $(TEOS)_{core}$ was prepared, but additionally APS was added after it was assumed that all TEOS was hydrolyzed and condensed, forming silica nanoparticles. No further adjustment during preparation was done. The molar ratio of TEOS to APS for the $(TEOS)_{core}(APS)_{shell}$ nanoparticle was 60, and the ratio was chosen based on previous nanoparticle preparation experience. The addition of APS did not break the stabilized micro emulsion state, as indicated by no apparent change in turbidity. It was assumed that APS was hydrolyzed inside the water droplet and then condensed onto the existing silica nanoparticle core. In preparation of the next nanoparticle, $(TEOS+APS)_{core}$, both APS and TEOS were added at the same time, after the reverse micro emulsion droplet was created. The molar ratio of TEOS to APS for the $(TEOS+APS)_{core}$ nanoparticle was 30. Based on this ratio, it was assumed that the TEOS

was evenly condensed across the whole structure of the silica nanoparticle, and that APS was also condensed across the entire structure of the silica nanoparticle, though at a lower percentage than TEOS. The amount of APS on the nanoparticle surface, therefore, should be negligible. Compared to the emulsion during the $(TEOS)_{core}$ nanoparticle synthesis, the solution showed a little more turbidity, but no disruption of the emulsion state, which usually can be easily noted by aggregation and sedimentation. The last nanoparticle, $(TEOS+APS)_{core}(APS)_{shell,}$ consists of the mixture of APS and TEOS inside the nanoparticle and APS shell on the surface. The total molar ratio of TEOS to APS is 22, and again no disruption of the emulsion state was observed. No additional ammonium hydroxide was added except prior to the addition of the precursor molecule. For all nanoparticles, after the hydrolysis and condensation of the TEOS and APS molecules, the emulsion state was broken by the addition of ethanol and any unreacted molecules, organic solvent, and surfactants were washed away through the purification. The final product was stored in 99% ethanol, and during the storage no significant sedimentation was observed, which is an indication of colloidal stability. For the sample preparation where the characterization method required a large mass of product, such as BET surface area measurement, the entire solution volume and corresponding precursor reagents were increased up to 4 times higher than the volume scale reported in the

method section, but there was no physical difference in final product, and no noticeable difference during preparation were observed. It was found that variation in which point during the synthesis APS is added influences the homogeneity of nanoparticle size production (ESI Fig. S1 to S5).

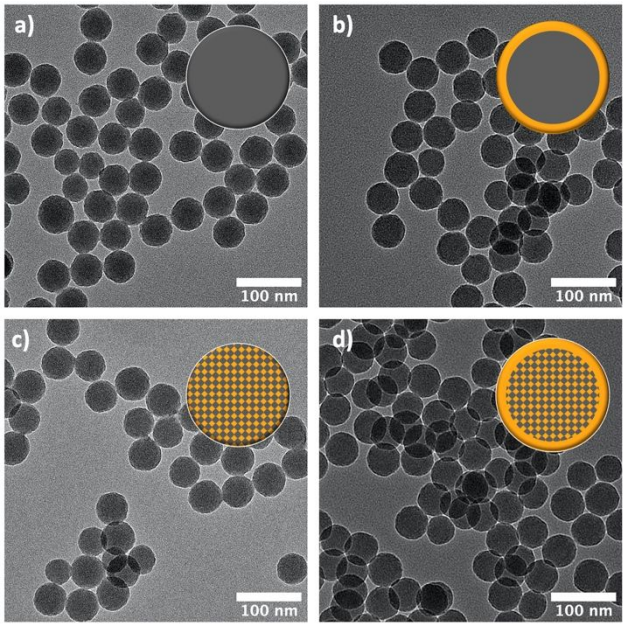

Fig. 1. Representative TEM images and graphical descriptions of the four different particles: a) $(TEOS)_{core}$, b) $(TEOS)_{core}(APS)_{shell}$, c) $(TEOS+APS)_{core}$ and d) $(TEOS+APS)_{core}(APS)_{shell}$. In the graphical descriptions, gray-colored areas indicate the location where TEOS is condensed, and

orange-colored areas indicate the location where APS is condensed. The molar ratio of TEOS and APS applied during particle preparation is not reflected in the schematics.

Table 1. Average diameters and number of particles measured from TEM images of each nanoparticle type and the zeta potentials of each particle in ethanol.

	Average diameter (nm)	Number of particles measured	Zeta potentials (mV)
$(TEOS)_{core}$	46.4 ± 6.3	481	-51.58 ± 1.78
$(TEOS)_{core}(APS)_{shell}$	48.6 ± 7.4	478	51.68 ± 1.56
$(TEOS+APS)_{core}$	49.3 ± 5.9	527	-30.04 ± 3.92
$(TEOS+APS)_{core}(APS)_{shell}$	48.5 ± 5.4	468	31.96 ± 1.84

The size and the morphology of each nanoparticle were analyzed via TEM. As shown in Fig. 1, all particles showed spherical shape as expected. For all particles, no noticeable density difference between the shell region and the core part was observed based on TEM contrast. The nanoparticles in Fig. 1 were originally dispersed in ethanol, and no hydrolysis, thus, degradation, was expected and all particles seem to display a solid spherical morphology, which is defined in this study as possessing no porosity above 3 nm in diameter. These similarities are ideal for comparing the different nanoparticle groups. The sizes of each nanoparticle in TEM images were measured to

obtain statistical size distribution, and that summary is listed in Table 1. The plot showing the size distribution for each nanoparticle type is in the ESI ($n > 400$, measured with ImageJ software). All four nanoparticle groups have similar average diameters and standard deviations, indicating that they possess similar physical characteristics in terms of size and morphology. The zeta potential values measured confirm that for $(TEOS+APS)_{core}$ there is not a significant amount of APS, which should induce positive surface electric potential, on the nanoparticle surface. Also, when APS is added later during the preparation, the APS molecules were successfully condensed on the surface, resulting in positive zeta potentials. Furthermore, the additional silica layer from APS did not generate a significantly increased diameter compared to the $(TEOS)_{core}$ or $(TEOS+APS)_{core}$ nanoparticles. The solid state NMR of $(TEOS+APS)_{core}$ confirms the existence of APS inside the silica nanoparticles (ESI, S6). Together, these characterizations prove that the nanoparticles' surface/chemical functionalization was done properly and that they share very similar physical characteristics.

From a previous study, it was noticed that the addition of APS within the traditional silica nanoparticles, which contains only TEOS as precursor molecules, leads to much more rapid

hydrolysis behavior and severe morphology change after dissolution.[26] This phenomenon was hypothesized to be due to the amine group on the APS molecule having a catalytic effect, breaking the siloxane bond when in aqueous media. Considering that APS is likely to catalyze the hydrolysis of siloxane bonds nearby, it is reasonable to speculate that APS on the outer surface of the nanoparticle may induce different dissolution behavior compared to the traditional silica nanoparticles. Although different reaction mechanisms have been proposed,[23,37] one of the most likely hydrolysis pathways is the breaking of the siloxane bond via hydroxide ion, creating a localized basic environment near the propyl amine functional group of APS, resulting in a more rapid dissolution of the silica nanoparticle (ESI, S7).

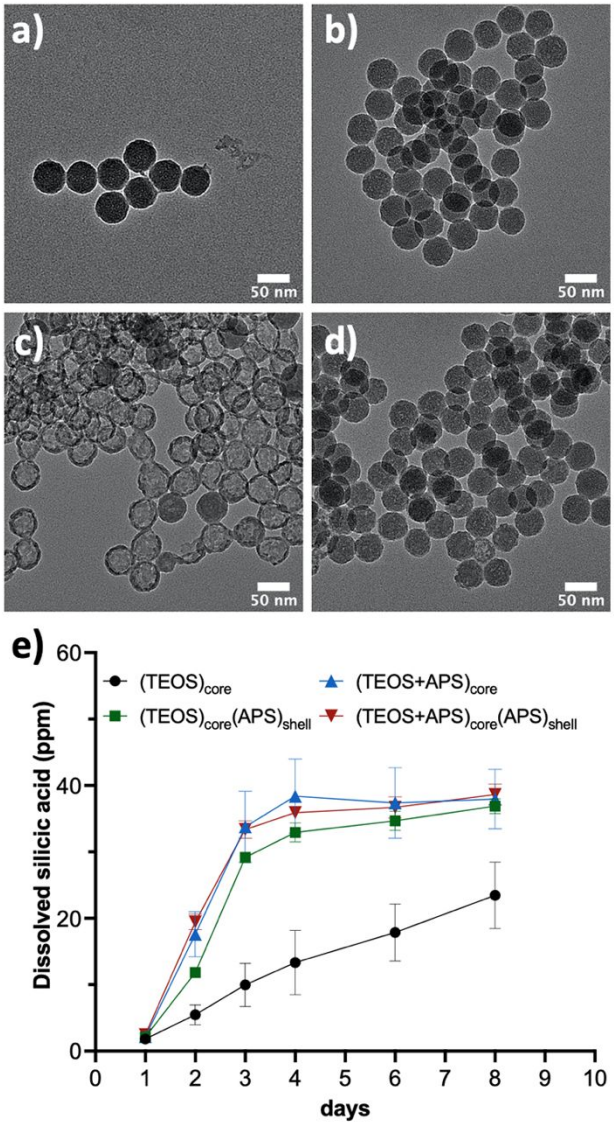

Fig 2. Representative TEM images of four particles after dissolution: a) $(TEOS)_{core}$ b) $(TEOS)_{core}(APS)_{shell}$ c) $(TEOS+APS)_{core}$ d) $(TEOS+APS)_{core}(APS)_{shell}$. e) Cumulative dissolved silicic acid concentration from the suspension of each particle in water measured using the silicomolybdic acid (SMA) spectrophotometric assay. The error bars represent the standard

deviation from 3 sample replicate. The nanoparticles in the TEM images were collected at the day 4 timepoint, and the concentration of all suspension was 100 ppm in pure water.

To investigate the dissolution behaviors of each nanoparticle type, the four different particles were dispersed in water at a concentration of 0.1 mg/mL. During incubation at room temperature, an aliquot was removed to measure the amount of dissolved silicic acid. The silicomolybdic acid (SMA) spectrophotometric assay can detect monomeric or oligomeric silicic acid dissolved from silica nanoparticles due to hydrolysis. The results in Fig. 2 show that all particles containing APS showed much more rapid dissolution than $(TEOS)_{core}$. It has been established that the solubility of orthosilicic acid (SiO_4H_4) is about 120 ppm at ambient temperature.[38] The amount of TEOS subjected to hydrolysis in this experiment should be below the solubility limit for all particles. For the $(TEOS)_{core}$ nanoparticles, which have the highest amount of TEOS per mass unit, in the concentration of 100 mg/L, 100% of the mass comes from TEOS. If it is assumed that all TEOS hydrolyzes and dissolves, the concentration of silicic acid would be 104.4 mg/L, which is a little lower than the solubility limit. Furthermore, the mass percentage of TEOS in $(TEOS+APS)_{core}(APS)_{shell}$, which has the lowest amount of TEOS per mass, is 93.7% and if all the TEOS from $(TEOS+APS)_{core}(APS)_{shell}$ dissolves, the concentration for the silicic acid would be

97.8 mg/L, only about 7 ppm different from that of $(TEOS)_{core}$. Despite the small difference in total dissolvable TEOS amounts between $(TEOS)_{core}$ and $(TEOS+APS)_{core}$, for example, Fig. 2e shows the dissolved silicic acid of 5.5 ppm and 17.6 ppm, respectively on day 2. Thus, the dissolved silicic acid concentration is more than 3 times higher in $(TEOS+APS)_{core}$ suspension, and it is reasonable to argue that the rapid dissolution from the silica nanoparticles containing APS is not caused by other factors such as different amount of TEOS in the nanoparticles or the solubility limit, but mainly due to the catalytic effect from APS.

It can also be found that even though dissolution is not as rapid as the $(TEOS+APS)_{core}$ or $(TEOS+APS)_{core}(APS)_{shell}$ nanoparticles, the $(TEOS)_{core}(APS)_{shell}$ formulation dissolved and released silicic acid much faster than the traditional $(TEOS)_{core}$ nanoparticles, indicating that the APS on the surface also facilitated breaking of the siloxane bonds. Interestingly, at first glance, the TEM images after dissolution do not look well-correlated with the SMA assay results. Fig. 2c shows the $(TEOS+APS)_{core}$ nanoparticles after dissolution for 96 hours, and the morphology has been changed to a hollow structure, unlike the $(TEOS)_{core}$ or $(TEOS)_{core}(APS)_{shell}$ formulations, which maintained their original solid spherical morphologies. For the $(TEOS+APS)_{core}$ nanoparticles, the outer region was maintained, resulting in hollow structures. This may be

attributed to the presence of APS mostly in the inner region of the nanoparticle, facilitating hydrolysis of siloxane bonds. Two possible contributors to this incomplete dissolution of the silica are that the system had not reached equilibrium and that the degree of condensation might be different in the interior and exterior regions, with the inner region having less complete condensation. The $(TEOS)_{core}(APS)_{shell}$ nanoparticles, where most of the APS is located on the nanoparticle exterior, did not transform into a hollow structure, but still released a significant amount of silicic acid, suggesting that the many siloxane bonds on the surface were hydrolyzed due to the presence of APS. These data suggest that the location of APS within the nanoparticle is likely more important than the degree of condensation. Based on these two nanoparticles' dissolution behaviors, it was initially hypothesized that the $(TEOS+APS)_{core}(APS)_{shell}$ nanostructure would dissolve at a much more rapid rate, achieving more complete dissolution. However, the TEM image in Fig. 2d shows that the inner region of the particle remains relatively unaffected, and the silicic acid release rate, which was similar to that of the $(TEOS+APS)_{core}$ nanostructure, was mainly caused by hydrolyzed TEOS from the nanoparticle exterior. This surface hydrolysis was confirmed by size analysis of TEM images measured after dissolution. In Fig. 3, the nanoparticles with APS on the surface showed a significant decrease in diameter

compared to the $(TEOS+APS)_{core}$ nanoparticles, which supports the fact that the $(TEOS+APS)_{core}$ hydrolysis occurs mostly in the nanoparticle interior. Solid-state silicon NMR spectra of post-aging $(TEOS+APS)_{core}$ showed that the degree of condensation was changed after the hydrolysis (ESI, S6).

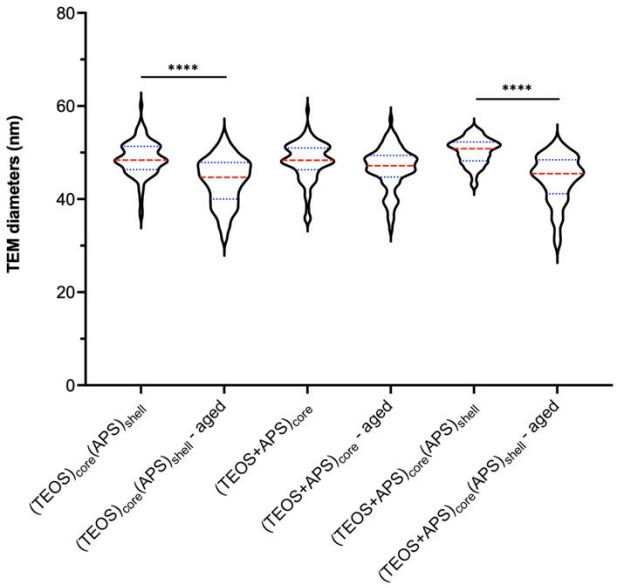

Fig. 3. Violin plot of TEM diameter measurement of the three particles before and after the dissolution (representative TEM images in Figure 2). The redline represents the median, the blue lines represent the lower quartile and upper quartile, respectively. The width of the curve represents approximate relative frequency of data points in each diameter region. The statistical significance

testing was performed via a one-way ANOVA with Tukey's multiple comparisons test to see the size change after dissolution: ****$p < 0.0001$.

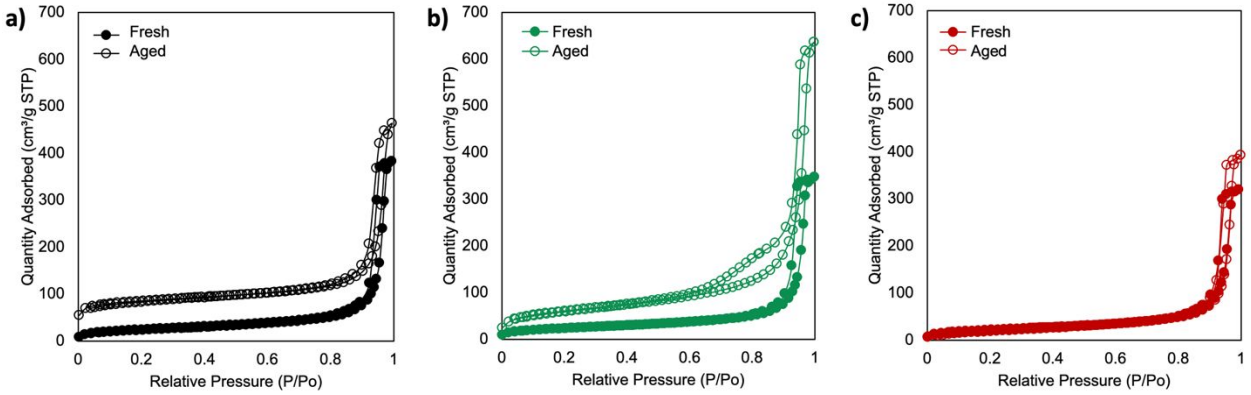

Fig 4. BET nitrogen adsorption and desorption isotherm plots for the three nanoparticles before and after incubation in water at a concentration of 100 ppm for 7 days. a) $(TEOS)_{core,}$ b) $(TEOS+APS)_{core,}$ and c) $(TEOS+APS)_{core}(APS)_{shell}$.

Table 2. BET surface area and pore volumes of the three particles before and after the incubation in water at a concentration of 100 ppm for 7 days, derived from isotherms showing in Figure 4.

	fresh BET surface area (m^2/g)	fresh pore volumes (cm^3/g) (1.9 - 3 nm)	fresh pore volumes (cm^3/g)	aged BET surface area (m^2/g)	aged pore volumes (cm^3/g) (1.9 - 3 nm)	aged pore volumes (cm^3/g)	Δpore volumes (cm^3/g) (1.9 - 3 nm)	ΔBET surface area (m^2/g)
$(TEOS)_{core}$	83.0	0.0098	0.53	207.7	0.029	0.98	196%	150%
$(TEOS+APS)_{core}$	82.1	0.0096	0.59	271.9	0.033	0.72	244%	231%
$(TEOS+APS)_{core}(APS)_{shell}$	75.5	0.0091	0.50	77.8	0.0093	0.61	2%	3%

To further investigate the physical change in each nanoparticle type after dissolution, nitrogen adsorption-desorption measurements were performed. The surface area and pore volume of the $(TEOS)_{core}$, $(TEOS+APS)_{core,}$ and $(TEOS+APS)_{core}(APS)_{shell}$ nanoparticles were measured and compared. As shown in Fig. 4 and Table 2, all three nanoparticles' surface area and pore volume increased after dissolution, but the degree of change was quite different among the different nanostructures. First, the surface area of $(TEOS)_{core}$ nanostructure increased 150% due to hydrolysis. From the isotherm plot, no noticeable hysteresis can be seen, and this indicates that this increased surface area was mainly due to increased porosity on the surface and the nanoparticle interior. This is further supported by an overall increase in pore volume from 0.53 to 0.98 cm^2/g. Additionally, the pore volume change in the small pore size region (1.9 to 3 nm) showed an

increase of 196%, which indicates that the nanoparticles experienced hydrolysis throughout the entire nanostructure. The $(TEOS+APS)_{core}$ nanostructure showed the most significant change in surface area, and this change was confirmed also by the obvious hysteresis in the isotherm plot between the 0.6 to 0.9 relative pressure region, indicating the hollow structure of the nanoparticles. However, the overall pore volume change was smaller than that of the $(TEOS)_{core}$ nanostructure, as the change resulted in about 35-40 nm macroporous hollow structure, which eliminated the possibility of forming a mesoporous structure (with smaller, nanometer-scale pores), which would be the major surface area contributor for the nanoparticle. Interestingly, the $(TEOS+APS)_{core}(APS)_{shell}$ nanostructure showed the least change among three. From the isotherm plot, no new hysteresis nor clear increased adsorbed nitrogen was observed, and as shown in Table 2, both pore volume in the small nanometer pore range as well as surface area increased only about 2 to 3%. This indicates that this nanoparticle did not dissolve much in the interior region. This was even lower than the theoretical surface area change with the assumption that no density change occurred when the nanoparticle diameter changes from 50.2 nm to 44.3 nm as measured from TEM images (calculated to be approximately a 13% decrease). It was unexpected that the $(TEOS+APS)_{core}(APS)_{shell}$ nanostructure showed an even lower degree of change than the

traditional $(TEOS)_{core}$ nanostructure, which released the least amount of silicic acid to media. The experimental and analytical errors during BET measurement should be considered, but even with that being considered, it is still clear that the interior region of the $(TEOS+APS)_{core}(APS)_{shell}$ nanostructures degraded much less than the traditional $(TEOS)_{core}$. This result suggests that the catalytic effect of APS on breaking siloxane bond in the interior region was suppressed to a great degree when there was APS on the surface of the nanoparticle as well, and this observation matches well with the TEM images of the nanoparticles measured in Fig 2d.

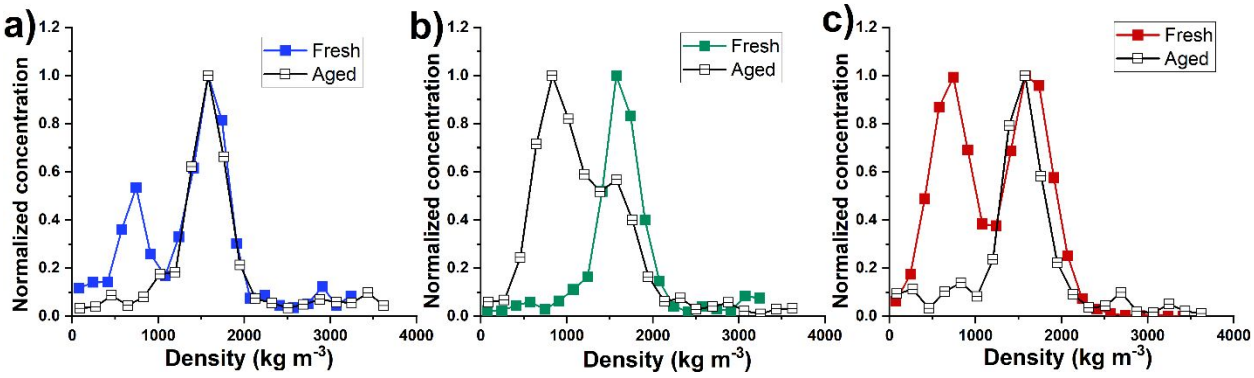

Fig. 5. The normalized nanoparticle density distribution for three particles as a function of density before (fresh) and after dissolution (aged 3 days). a) $(TEOS)_{core}(APS)_{shell}$, b) $(TEOS+APS)_{core}$, and

c) $(TEOS+APS)_{core}(APS)_{shell}$. Density distributions correspond to the mode mobility diameter for each distribution.

Nanoparticle density distributions measurements are an additional method to assess degradation. TEM measurements are somewhat limited in their ability to estimate the density of the nanoparticles; this is because TEM depends on contrast, and contrast is a relative measurement to the background. Depending on the experimental procedure and material, the darkness of the nanoparticle in bright-field TEM may vary. BET measurement also presents limited utility for assessing density because it assumes that the powdered nanoparticles are one big homogenous matrix, and information on the single nanoparticle level is inaccessible. Therefore, we utilized aerosol IM-MS to examine the density distributions of the $(TEOS)_{core}(APS)_{shell}$, $(TEOS+APS)_{core}$, and $(TEOS+APS)_{core}(APS)_{shell}$ nanostructures. Prior to aerosol IMS, SMPS measurements (Fig. S8) revealed that the mode mobility diameters for aerosolized $(TEOS)_{core}(APS)_{shell}$, $(TEOS+APS)_{core}$, and $(TEOS+APS)_{core}(APS)_{shell}$ were all near 57.2 nm, decreasing to 55.2 nm after aging. In all distributions, there was a second peak in the 30-50 nm range as well. The larger mobility diameters than observed via TEM and second peak are attributable to non-volatile residue in aerosolized

droplets; droplet devoid of a silica nanoparticle leave a smaller residue particle, while droplets containing a silica nanoparticle have a residue coating on the particle, increasing the diameter from the true diameter. Nonetheless, the presence of non-volatile residue on particles does not preclude the use of aerosol IM-MS to infer density distributions, as changes in density are still detectable. Fig. 5a shows the density distribution of the $(TEOS)_{core}(APS)_{shell}$ nanoparticles prior to dissolution and post degradation; in both instances, nanoparticles of the peak (mode) mobility diameter were selected by the DMA, and the APM was stepped to examine particle mass distributions. The resulting bimodal distribution for the unaged sample arises from non-volatile residue particles, and is not considered in analysis. The main density peak, with a density near 1.6 g cm^{-3}, is attributable to the silica nanoparticles, and there is little-to-no change in the density distribution upon sample aging. In contrast, examining similar results for the $(TEOS+APS)_{core}$ nanostructures in Fig. 5b, there is a reduction clear shift in the peak density, indicative of dissolution. As this shift corresponds to particles of the mode mobility diameter, presumably, the decrease in density is attributable to the formation of hollow particles of the nanostructure. Finally, in Fig. 5 c, the nanoparticle density distribution for the $(TEOS+APS)_{core}(APS)_{shell}$ nanoparticle also shows a clear bimodal distribution prior to dissolution, due to non-volatile residue particles. However, upon agin,

while a shift to lower densities is evident, this shift is much smaller than observed for the $(TEOS+APS)_{core}$ nanostructures.

The combined analyses performed suggests two important events regarding the colloidal stability of silica nanoparticles. First, APS on the surface is highly reactive, and the stability of this surface functionalization should be evaluated carefully. Secondly, APS on the surface prevented APS-induced catalytic hydrolysis dissolution behavior in the nanoparticle interior. This was surprising as the initial hypothesis was that if there was additional APS on the surface, it might cause the complete dissolution of the nanoparticle instead of forming a hollow structure. This was APS-specific behavior: when other silica precursor molecules, such as TEOS, TMS or PEG were added on the surface of the $(TEOS+APS)_{core}$ nanoparticle, no suppression of interior dissolution occurred (ESI, S8). It is carefully inferred from the results of this study that this APS-induced dissolution behavior might be related to the regional pH. Propyl amine is a weak base, with a pK_b of around 3 to 4.[39] In neutral pH aqueous solutions, the amine group is in a protonated state with a positive charge, and OH- would be produced upon interaction with water molecules. Perhaps, it is this hydroxide ion that induces rapid hydrolysis of the siloxane bonds. When APS is located in

two different regions of the nanoparticles, it is likely that APS on the surface is protonated first, generating OH-. This would make the media around the nanoparticles basic, but APS in the nanoparticle interior then acts as acid, removing the OH- in the interior region and slowing down the hydrolysis. To probe this speculation, another experiment was conducted wherein three nanoparticles: $(TEOS)_{core}$, $(TEOS+APS)_{core,}$ and $(TEOS+APS)_{core}(APS)_{shell}$ were dispersed in basic aqueous solution at pH 11.4, and their morphology changes were measured via TEM (ESI, S9). As widely known from previous studies, traditional silica nanoparticles degrade and dissolve at a much faster rate in basic media,[40] and the suspension of $(TEOS)_{core}$ became transparent after incubation; only a small number of nanoparticles were imaged via TEM, showing severe degradation as expected. Surprisingly, the $(TEOS+APS)_{core}(APS)_{shell}$ nanostructure seemed intact, and little degradation took place. Furthermore, it was inferred from $(TEOS+APS)_{core}$ TEM images that the outer region where APS is almost absent was significantly degraded, but the interior, where APS is located, remained relatively intact. From the dissolution images recorded for all three nanoparticles, it can be concluded that the APS-laden regions of the nanoparticles were not degraded; this result agrees with all data reported herein if it is assumed that APS can locally neutralize high pH in basic conditions, protecting the nanoparticles from rapid hydrolysis.

Conclusion

Monodispersity and colloidal stability are two critical factors that determine nanomaterials' potential and performance. Many applications involve surface functionalization of nanoparticles as an essential part of preparation, and APS has been applied to silica nanoparticle in various studies to effectively enhance the nanoparticles' functionality. Data about the stability of the functionalization and how APS-functionalized nanoparticles degrade are largely unavailable. This study shows that the regional localization of APS on/in silica nanoparticles can dramatically change the nanoparticles' dissolution, likely impacting a nanoparticle's functionality. The distinct nanostructures designed and synthesized herein using reverse micro emulsion clearly demonstrates that APS functionalization can facilitate the hydrolysis of the nanoparticles, and in some cases, decelerate it, depending on the media and how the nanoparticles are prepared. The understanding gained herein will be used for developing more effective and robust silica nanoparticle preparations for various applications.

Acknowledgement

This material is based upon work supported by the National Science Foundation under Grant No. CHE-2001611, the NSF Center for Sustainable Nanotechnology (CSN). The CSN is part of

the Centers for Chemical Innovation Program. Parts of this work, especially TEM characterization, were carried out in the Characterization Facility at the University of Minnesota, which receives partial support from NSF through the MRSEC program (DMR-1420013). This work was also supported by the National Institutes of Health Biotechnology Training Grant to T.L.O. (Grant T32-GM008347). Measurement of the silicon solid state NMR data found in the SI was performed by Dr. Alejandro Vidal, Dr. Carla Maria Vidaurre Agut, and Prof. Pablo Botella Asunción at Instituto de Tecnología Química, Universitat Politècnica de València-Consejo Superior de Investigaciones Científicas. Aerosol IM-MS measurements were supported by NSF Grant No. 2002852.

Reference

1. Argyo C, Weiss V, Bräuchle C, Bein T. Multifunctional Mesoporous Silica Nanoparticles as a Universal Platform for Drug Delivery. Chem Mater. 2014 Jan 14;26(1):435–51.

2. Bharti C, Gulati N, Nagaich U, Pal A. Mesoporous silica nanoparticles in target drug delivery system: A review. Int J Pharma Investig. 2015;5(3):124.

3. Vallet-Regí M, Colilla M, Izquierdo-Barba I, Manzano M. Mesoporous Silica Nanoparticles for Drug Delivery: Current Insights. Molecules. 2017 Dec 25;23(1):47.

4. Cha BG, Kim J. Functional mesoporous silica nanoparticles for bio-imaging applications. WIREs Nanomed Nanobiotechnol [Internet]. 2019 Jan [cited 2021 Dec 20];11(1). Available from: https://onlinelibrary.wiley.com/doi/10.1002/wnan.1515

5. Dogra P, Adolphi NL, Wang Z, Lin YS, Butler KS, Durfee PN, et al. Establishing the effects of mesoporous silica nanoparticle properties on in vivo disposition using imaging-based pharmacokinetics. Nat Commun. 2018 Dec;9(1):4551.

6. Lin YS, Abadeer N, Hurley KR, Haynes CL. Ultrastable, Redispersible, Small, and Highly Organomodified Mesoporous Silica Nanotherapeutics. J Am Chem Soc. 2011 Dec 21;133(50):20444–57.

7. Rosenholm JM, Meinander A, Peuhu E, Niemi R, Eriksson JE, Sahlgren C, et al. Targeting of Porous Hybrid Silica Nanoparticles to Cancer Cells. ACS Nano. 2009 Jan 27;3(1):197–206.

8. Wang LS, Wu LC, Lu SY, Chang LL, Teng IT, Yang CM, et al. Biofunctionalized Phospholipid-Capped Mesoporous Silica Nanoshuttles for Targeted Drug Delivery: Improved Water Suspensibility and Decreased Nonspecific Protein Binding. ACS Nano. 2010 Aug 24;4(8):4371–9.

9. Brevet D, Gary-Bobo M, Raehm L, Richeter S, Hocine O, Amro K, et al. Mannose-targeted mesoporous silica nanoparticles for photodynamic therapy. Chem Commun. 2009;(12):1475.

10. Wilhelm S, Tavares AJ, Dai Q, Ohta S, Audet J, Dvorak HF, et al. Analysis of nanoparticle delivery to tumours. Nat Rev Mater. 2016 May;1(5):16014.

11. Buchman JT, Elmer WH, Ma C, Landy KM, White JC, Haynes CL. Chitosan-Coated Mesoporous Silica Nanoparticle Treatment of *Citrullus lanatus* (Watermelon): Enhanced Fungal Disease Suppression and Modulated Expression of Stress-Related Genes. ACS Sustainable Chem Eng. 2019 Dec 16;7(24):19649–59.

12. Rastogi A, Tripathi DK, Yadav S, Chauhan DK, Živčák M, Ghorbanpour M, et al. Application of silicon nanoparticles in agriculture. 3 Biotech. 2019 Mar;9(3):90.

13. Rajput VD, Minkina T, Feizi M, Kumari A, Khan M, Mandzhieva S, et al. Effects of Silicon and Silicon-Based Nanoparticles on Rhizosphere Microbiome, Plant Stress and Growth. Biology. 2021 Aug 17;10(8):791.

14. Moitra N, Ichii S, Kamei T, Kanamori K, Zhu Y, Takeda K, et al. Surface Functionalization of Silica by Si–H Activation of Hydrosilanes. J Am Chem Soc. 2014 Aug 20;136(33):11570–3.

15. Le VN, Rui Y, Gui X, Li X, Liu S, Han Y. Uptake, transport, distribution and Bio-effects of SiO2 nanoparticles in Bt-transgenic cotton. J Nanobiotechnol. 2014 Dec;12(1):50.

16. Blanco E, Shen H, Ferrari M. Principles of nanoparticle design for overcoming biological barriers to drug delivery. Nat Biotechnol. 2015 Sep;33(9):941–51.

17. Miranda A, Martínez L, De Beule PAA. Facile synthesis of an aminopropylsilane layer on Si/SiO2 substrates using ethanol as APTES solvent. MethodsX. 2020;7:100931.

18. Kardys AY, Bharali DJ, Mousa SA. Amino-Functionalized Silica Nanoparticles: In Vitro Evaluation for Targeted Delivery and Therapy of Pancreatic Cancer. Journal of Nanotechnology. 2013;2013:1–8.

19. Mohammadnezhad G, Dinari M, Soltani R. The preparation of modified boehmite/PMMA nanocomposites by in situ polymerization and the assessment of their capability for Cu^{2+} ion removal. New J Chem. 2016;40(4):3612–21.

20. Rajan R, Rainosalo E, Thomas SP, Ramamoorthy SK, Zavašnik J, Vuorinen J, et al. Modification of epoxy resin by silane-coupling agent to improve tensile properties of viscose fabric composites. Polym Bull. 2018 Jan;75(1):167–95.

21. Shafqat SS, Khan AA, Zafar MN, Alhaji MH, Sanaullah K, Shafqat SR, et al. Development of amino-functionalized silica nanoparticles for efficient and rapid removal of COD from pre-treated palm oil effluent. Journal of Materials Research and Technology. 2019 Jan;8(1):385–95.

22. Cuoq F, Masion A, Labille J, Rose J, Ziarelli F, Prelot B, et al. Preparation of amino-functionalized silica in aqueous conditions. Applied Surface Science. 2013 Feb;266:155–60.

23. Asenath Smith E, Chen W. How To Prevent the Loss of Surface Functionality Derived from Aminosilanes. Langmuir. 2008 Nov 4;24(21):12405–9.

24. Kanan SM, Tze WTY, Tripp CP. Method to Double the Surface Concentration and Control the Orientation of Adsorbed (3-Aminopropyl)dimethylethoxysilane on Silica Powders and Glass Slides. Langmuir. 2002 Aug 1;18(17):6623–7.

25. Lin CH, Chang JH, Yeh YQ, Wu SH, Liu YH, Mou CY. Formation of hollow silica nanospheres by reverse microemulsion. Nanoscale. 2015;7(21):9614–26.

26. Kang H, Elmer W, Shen Y, Zuverza-Mena N, Ma C, Botella P, et al. Silica Nanoparticle Dissolution Rate Controls the Suppression of *Fusarium Wilt* of Watermelon (*Citrullus lanatus*). Environ Sci Technol. 2021 Oct 19;55(20):13513–22.

27. Finnie KS, Bartlett JR, Barbé CJA, Kong L. Formation of Silica Nanoparticles in Microemulsions. Langmuir [Internet]. 2007 Mar [cited 2020 Mar 1];23(6):3017–24. Available from: https://pubs.acs.org/doi/10.1021/la0624283

28. Coradin T, Eglin D, Livage J. The silicomolybdic acid spectrophotometric method and its application to silicate/biopolymer interaction studies. Spectroscopy [Internet]. 2004 [cited 2019 Nov 12];18(4):567–76. Available from: http://www.hindawi.com/journals/jspec/2004/356207/abs/

29. Jeon S, Oberreit DR, Van Schooneveld G, Gao Z, Bischof JC, Haynes CL, et al. Ion-Mobility-Based Quantification of Surface-Coating-Dependent Binding of Serum Albumin to Superparamagnetic Iron Oxide Nanoparticles. ACS Appl Mater Interfaces. 2016 Sep 21;8(37):24482–90.

30. Li C, Lee AL, Chen X, Pomerantz WCK, Haynes CL, Hogan CJ. Multidimensional Nanoparticle Characterization through Ion Mobility-Mass Spectrometry. Anal Chem. 2020 Feb 4;92(3):2503–10.

31. Lee J, He S, Song G, Hogan CJ. Size distribution monitoring for chemical mechanical polishing slurries: An intercomparison of electron microscopy, dynamic light scattering, and differential mobility analysis. Powder Technology. 2022 Jan;396:395–405.

32. Wang SC, Flagan RC. Scanning Electrical Mobility Spectrometer. Aerosol Science and Technology. 1990 Jan;13(2):230–40.

33. Shimada M, Han B, Okuyama K, Otani Y. Bipolar Charging of Aerosol Nanoparticles by a Soft X-ray Photoionizer. JOURNAL OF CHEMICAL ENGINEERING OF JAPAN. 2002;35(8):786–93.

34. Chen DR, Pui DYH, Hummes D, Fissan H, Quant FR, Sem GJ. Design and evaluation of a nanometer aerosol differential mobility analyzer (Nano-DMA). Journal of Aerosol Science. 1998 Jun;29(5–6):497–509.

35. Tajima N, Sakurai H, Fukushima N, Ehara K. Design Considerations and Performance Evaluation of a Compact Aerosol Particle Mass Analyzer. Aerosol Science and Technology. 2013 Oct;47(10):1152–62.

36. Tajima N, Fukushima N, Ehara K, Sakurai H. Mass Range and Optimized Operation of the Aerosol Particle Mass Analyzer. Aerosol Science and Technology. 2011 Feb;45(2):196–214.

37. Mashhadizadeh MH. Drug-Carrying Amino Silane Coated Magnetic Nanoparticles as Potential Vehicles for Delivery of Antibiotics. J Nanomedic Nanotechnol [Internet]. 2012 [cited 2022 May 7];03(04). Available from: https://www.omicsonline.org/drug-carrying-amino-silane-coated-magnetic-nanoparticles-as-potential-vehicles-for-delivery-of-antibiotics-2157-7439.1000139.php?aid=7011

38. Pradeep K, Nepolian M, Anandhan P, Chandran, Kaviyarasan R, Prasanna MV, et al. A study on variation in dissolved silica concentration in groundwater of hard rock aquifers in Southeast coast of India. IOP Conf Ser: Mater Sci Eng. 2016 Mar;121:012008.

39. Rani D, Rollo S, Olthuis W, Krishnamoorthy S, Pascual García C. Combining Chemical Functionalization and FinFET Geometry for Field Effect Sensors as Accessible Technology to Optimize pH Sensing. Chemosensors. 2021 Jan 21;9(2):20.

40. Brinker CJ. Hydrolysis and condensation of silicates: Effects on structure. Journal of Non-Crystalline Solids. 1988 Mar;100(1–3):31–50.